

# Intelligent upper-limb exoskeleton using deep learning to predict human intention for sensory-feedback augmentation

Jinwoo Lee<sup>1,2,†</sup>, Kangkyu Kwon<sup>2,3,†</sup>, Ira Soltis<sup>2,4,†</sup>, Jared Matthews<sup>2,4</sup>, Yoonjae Lee<sup>2,3</sup>, Hojoong Kim<sup>2,4</sup>, Lissette Romero<sup>2,5</sup>, Nathan Zavanelli<sup>2,3</sup>, Youngjin Kwon<sup>2,4</sup>, Shinjae Kwon<sup>2,4</sup>, Jimin Lee<sup>2,4</sup>, Yewon Na<sup>2,4</sup>, Sung Hoon Lee<sup>2,3</sup>, Minoru Shinohara<sup>2,6,7</sup>, Frank L. Hammond<sup>4,7</sup>, Woon-Hong Yeo<sup>2,4,7,8\*</sup>

<sup>1</sup> Department of Mechanical, Robotics, and Energy Engineering, Dongguk University, 30 Pildong-ro 1-gil, Jung-gu, Seoul, 04620, South Korea

<sup>2</sup> IEN Center for Human-Centric Interfaces and Engineering, Institute for Electronics and Nanotechnology, Georgia Institute of Technology, Atlanta, GA, 30332 USA

<sup>3</sup> School of Electrical and Computer Engineering, Georgia Institute of Technology, Atlanta, GA 30332, USA

<sup>4</sup> George W. Woodruff School of Mechanical Engineering, Georgia Institute of Technology, Atlanta, GA, 30332 USA

<sup>5</sup> School of Industrial Design, Georgia Institute of Technology, Atlanta, GA 30332, USA

<sup>6</sup> School of Biological Sciences, Georgia Institute of Technology, Atlanta, GA, 30332, USA

<sup>7</sup> Wallace H. Coulter Department of Biomedical Engineering, Georgia Institute of Technology and Emory University School of Medicine, Atlanta, GA, 30332 USA

<sup>8</sup> Institute for Materials, Parker H. Petit Institute for Bioengineering and Biosciences, Neural Engineering Center, Institute for Robotics and Intelligent Machines, Georgia Institute of Technology, Atlanta, GA, 30332 USA

† J. Lee, K. Kwon, and I. Soltis equally contributed to this work

\*Corresponding author. Email: Dr. Woon-Hong Yeo (whyeo@gatech.edu)

## Abstract

The age and stroke-associated decline in musculoskeletal strength and control affects a serious number of the global population since it impacts the functional independence of individuals with neuromotor disorders and degrades their capability to perform daily tasks using the upper extremities. Exoskeleton robots have been developed to address this issue, but the existing studies could not provide viable solutions in real-life situations mainly due to the absence of the human intention predicting platform, lack of sensory feedback, and incapability to support multiple joint movements of upper limbs. Here, this study proposes the intent-driven robotic exoskeleton that augments the human upper-extremity joint movements by the seamless integration of cloud-based human intention predicting deep-learning algorithm and skin-like bioelectronics for sensory feedback. To assist the upper-limb joint movements, we developed soft lightweight pneumatics that can provide 897 N of force and 78.7 mm of displacement at maximum such that contraction displacement can be translated to the exoskeleton via cable. The skin-like, wireless bioelectronics build sensory feedback by collecting real-time electromyography (EMG) signals, which are simultaneously cloud-computed to determine the user's intended movement. The cloud-based deep-learning classifications can predict four upper-limb joint movements with an average accuracy of 96.2% at a 200-250 ms response rate, suggesting that the exoskeleton operates just by human intention. Besides, the intent-driven exoskeleton can augment human strength by 5.15 times on average when compared to the unassisted mode without wearing the exoskeleton. In this regard, we expect that this study will offer a potent solution for the substantially large population with neuromotor disorders and further transform their lifestyles in near future.

## Introduction

An enormous number of individuals suffer from neuromotor disorders that primarily arise from stroke-induced and age-associated declines in musculoskeletal strength and control. Statistically, strokes affect one out of four adults over the age of 25 in their lifetime, and 12.2 million of the global population experience stroke each year<sup>1</sup>, resulting in neuromotor disorders for 20-40% of victims even if they manage to survive the strokes<sup>2</sup>. Thus, it is expected that the population with neuromotor disorders will amount to a much larger number if we also consider the elderly population with neuromotor disorders. Such a disorder restricts the functional independence of the afflicted population because the heavily reduced motor control and unwanted tremor of the upper limb usually pose considerable difficulties in performing everyday tasks that require the dexterity of the upper limbs. Moreover, neuromotor disorders usually generate a tremendous, yet necessary, amount of social expense in the healthcare system such as rehabilitation clinics or the constant presence of a caregiver. It is reported that the direct and indirect social costs resulting from stroke amount to approximately \$65 billion in the United States alone annually.<sup>3</sup>

There exists an immediate demand to address these problems, and the existing robots are capable of mechanically augmenting human upper-extremity strengths. However, the previously reported exoskeletons are not capable of providing pragmatic solutions for the population with neuromotor disorders because they lack essential functionalities to augment the upper-extremity movements in a user-friendly fashion. Primarily, the most critical limitation of the previous exoskeletons originates from their incapability to predict the real-time intention of the user.<sup>4-14</sup> In other words, many of the existing solutions can only assist the movements of the user only in the presence of the external pre-programmed inputs due to the absence of sensory feedback pathways and the artificial intelligence to predict the real-time intention of the user. These features of the previous works served to circumscribe practical use in real life due to their passive operational mode and functional inconvenience.

Another limitation of the previously reported exoskeletons for upper-extremity strength augmentation originates from their overall structure design. Many of the existing works are designed to be used only in a stationary manner, and such a design limits their potential use to assist the strength augmentation for conducting everyday tasks in a mobile style.<sup>4, 10, 15-18</sup> Moreover, a considerable number of exoskeletons rely on the complex hardware of large form factors with complicated electrical wiring, which make the users difficult to use and adapt to.<sup>6, 9, 10, 12, 16-18</sup> Besides the hardware design, a majority of the previous upper-extremity exoskeletons serve to assist only a single joint movement such as an elbow or shoulder joint movement<sup>4, 5, 7, 8, 13, 19</sup>, although many of the everyday tasks often demand the use of both elbow and shoulder joint movements along with combined movements of the two.

In addition to the exoskeleton hardware design, sensory haptic feedback in human assistive robotics is a crucial feature because it translates the human physiological signals into strength augmentation of an arbitrary movement. In this context, although other physiological signals such as electroencephalogram (EEG) can provide useful information about human intention<sup>20-22</sup>, EMG signals can offer more direct information about upper-extremity movements since they are associated with the electrical activity of the skeletal muscles. Nevertheless, some of the existing upper-extremity exoskeletons do not incorporate any physiological sensors<sup>4, 15, 19</sup>, and many of the previous works, which include EMG sensors in their systems, use the sensory information to compare the relative muscle involvement, rather than for the sensory feedback purpose<sup>5, 6, 8-14</sup>. Furthermore, some of the recent exoskeletons with sensory feedback utilize commercial EMG sensors that are based on wired and gel-type electrodes. However, commercial gel-type electrodes are reported to cause skin allergic

reactions when used for the long term due to the presence of acrylic acid in the gel<sup>23-25</sup>, and the tethered wires not only aggravate the mobility of the user but also cause motion artifacts based on the wire tension.

All of these critical limitations of the current upper-extremity exoskeletons - including the incapability to determine the user's intent, hardware design, and motion artifacts from commercial sensors - restrain the realistic use of exoskeletons in daily life. A recent innovative study by Georgarakis et al. demonstrated an exosuit that can assist the vertical shoulder flexion with sensory-haptic feedback for daily life applications<sup>19</sup>. Yet, the exosuit in this work can only support a single upper-extremity joint movement, even though more than one upper-extremity movement is required to conduct everyday tasks, so extensive opportunities to improve the current solutions still exist for the current generation of exoskeletons. In this respect, we believe that the ideal exoskeleton robot for human strength augmentation should be able to (i) predict the user's intended movement with high accuracy, (ii) be portable, (iii) be lightweight, (iv) be easy to use, (v) support the multiple upper-limb joint movements, and (vi) incorporate the high-fidelity sensory feedback with motion-artifact-free and non-allergic EMG signal sensors. In this respect, to the authors' best knowledge, there has been no work that totally integrated all the ideal elements into a fully functional exoskeleton that can assist individuals with the neuromotor disorder in performing everyday tasks in a completely user-friendly fashion.

In this study, we developed a human-intent-driven robotic exoskeleton that assists the upper-extremity joint movements by a deep-learning-based cloud computing platform with high-fidelity sensory feedback using soft bioelectronics. The incorporation of the deep-learning-based cloud computing platform into the human assistive robot enables the real-time prediction of the user's intended movement with high accuracy. Moreover, the wearable exoskeleton uses pneumatic artificial muscles (PAMs) to generate a high magnitude of mechanical force such that they can assist the multiple intended movements of the wearer. The portable and lightweight structure of the exoskeleton not only enhances the mobility of the wearer but also allows natural upper-extremity movements, delivering strength assistance while minimizing the form factor. Furthermore, we developed a wireless, artificial EMG-sensing skin that can monitor the high-quality electrophysiological signals in multi-channels to constitute reliable sensory feedback. Table 1 captures the novelty of this work by drawing a comparison between this work and the existing exoskeletons. The shaded boxes in the table indicate the ideal functionalities for the upper-extremity assistive exoskeleton, and the exoskeleton in this work is the only solution that satiates all the criteria for faithful and user-oriented human strength assistance.

## Results

**Figure 1** presents the general overview of the intent-driven exoskeleton robot that totally integrated the sensory feedback, human intent predicting algorithm, and strength augmenting robotics for assisting the upper-limb joint movements. The skin-like sensors attached to the wearer's skin acquire the EMG signals and wirelessly transmit the collected signals to the Android cloud in real-time. Thus, when the human wearer intends to perform an arbitrary joint movement by activating the associated upper-limb muscles, the multi-channel sensors simultaneously send the EMG signals to the cloud, which conducts the signal processing and the deep-learning algorithm to predict the intended movement. Then, the prediction output is wirelessly transferred to the exoskeleton such that the robot assists the intended movement in real-time. All these sequential processes occur within 350 ms, and the exoskeleton system in this work can support four upper-limb movements in total: shoulder flexion, shoulder extension, elbow flexion, and elbow extension, all of which are crucial joint movements to perform

everyday tasks in the real world. Thus, all the user needs to do is to intend to perform one of the upper-extremity joint movements, and the exoskeleton will start assisting the movement of the wearer by predicting the intended movement based on the onset of the specific muscle activation. All of this is possible due to the seamless integration of each component into the fully functional, all-in-one system.

**Figure 2** delineates the first component of the intent-driven exoskeleton, the PAM and exoskeleton frame, which serve to augment human upper-limb strength for supporting daily tasks. We employed soft pneumatics as a driving force for the system due to its desirable characteristics such as natural compliance, low power consumption, lightweight, high force-to-weight ratio, simple controllability, and inherently safe mechanism<sup>26-28</sup>. Hence, to deliver such benefits of soft pneumatics, we designed PAM that operates just like human muscles as in **Figure 2a**, which shows its contraction in the longitudinal direction and generates force as PAM inflates, converting the compressed air energy into mechanical motion. As can be seen from the exploded view of PAM in **Figure 2b**, the soft actuator inflates as the air is infused into its elastomeric silicone bladder via the pneumatic tube, and the polyester mesh sleeving serves to restrict the strain of PAM to a certain extent. **Figure 2c** characterizes the relationship between force and contraction length of a single PAM unit as the air pressure increases from 68.9 kPa (10 psi) to 551 kPa (80 psi). Through maximum strength testing, we found that forces above 900 N can cause the PAM to mechanically fail in a controlled manner. At such high forces, the silicone tubing is cut at the interface between the tubing and aluminum end fittings, which results in the high-pressure air leak out. As a result, the pressure range of the exoskeleton was set from 68.9 kPa (10 psi) to 414 kPa (60 psi), and a 483 kPa (70 psi) pressure relief valve was integrated for additional safety. Since the force-contraction profile retains an approximately linear relationship with constant pressure, this relationship can be used to provide the desired exoskeleton assistance force for a given joint angle. It is reported that approximately 10 to 15% of the body weight is needed to lift the arm vertically, so it would require 120 N for a person who weighs 80 kg to lift the arm<sup>29, 30</sup>. The result suggests that a single PAM can generate a far greater force for strength augmentation because it can produce 897 N and 87 mm of displacement at maximum, for a PAM with a bladder length of 34 cm, owing to the high force-to-weight ratio of soft pneumatics. A single PAM unit only weighs 104 g, and the exoskeleton system utilizes three PAMs to assist different upper-extremity joint movements. **Figure 2d** presents the exploded view of the exoskeleton and constituting components. The exoskeleton was constructed primarily out of carbon fiber with machined aluminum connectors and stainless steel bolts such that the exoskeleton would be strong, stiff, and lightweight (670g). The exoskeleton attaches to the backpack with a super swivel ball joint, which allows the exoskeleton to move naturally with the body. Carbon fiber twill weave telescoping tubing and two telescoping collet sets constitute the main vertical strut between the hip and shoulder joint and the strut between the shoulder and elbow joints. This method allows for easy exoskeleton adjustment to different subject body sizes (**Figure 2e**). Quick adjustments can be made to the hip-to-shoulder, shoulder-to-elbow, and elbow-to-wrist lengths, but creating a comfortable interface between the exoskeleton and the user can still present fitment challenges. Nevertheless, by leveraging 3D printing for the upper and lower arm mounts, both "one size fits all" as well as personalized arm mounts can be easily developed and bolted to the exoskeleton. In this design, the arm mounts are 3D printed as a flat pattern and hot water thermoformed ergonomically attach to the curved geometry of the arm. For additional arm mobility, an inline ball joint interfaces between the 3D-printed upper arm mount and the carbon fiber tubing. We placed the PAMs inside the backpack as in **Figure S1** such that PAMs do not interfere with the natural movements of the wearer while delivering the required augmentation



force via cables as PAMs contract. The backpack also contains compressor and solenoid valves that serve to infuse or remove air into/from each PAM unit rapidly, following the flow diagram and power diagram in **Figure S2** and **Figure S3** respectively. **Figure 2f** presents snapshots of the human subject wearing the integrated system of the exoskeleton and backpack. The integrated system, which also consists of a battery, cable, printed circuit board (PCB), and PAM frame, weighs only 4.7 kg, and the weight of each component is tabulated in **Table S1**. The moderate load of 4.7 kg should be carryable for a short period of time even for people with declined strength. The backpack distributes the load evenly across the shoulders and back, which can make it more stable and comfortable to carry than other methods. A study found that wearing a backpack with a load of up to 10% of body weight had no significant effect on gait or posture<sup>31</sup>. Thus, despite the extra weight of the exoskeleton that the wearer will have to carry, we believe that the moderate load of 4.7 kg should not inflict substantial discomfort on the target individuals. The PCB in the backpack enables wireless data acquisition from the Android cloud and provides mechanical force for strength augmentation by controlling the solenoid valves with MOSFETs as illustrated in **Figure S4**. In addition, the pressure sensor in the PCB monitors the pressure of each PAM in real-time such that the user can keep track of the input pressure with the portable device interface.

To incorporate the sensory feedback into the intent-driven exoskeleton, we developed a skin-like EMG sensor that can monitor the muscle activity signals wirelessly with minimized motion artifacts. **Figure 3a** illustrates the assembled and exploded view of the skin-like EMG sensor that mainly consists of stretchable gold/polyimide (PI) nanomembrane electrodes, a silicone-based adhesive patch, a PI flexible circuitry, and a customized magnet-chargeable battery that can be switched on and off. The skin-like sensor developed herein can be attached to the skin surface just as a thin-film adhesive patch due to its extremely small form factor and lightweight nature as presented in **Figure 3b**. Unlike the commercial sensor that uses the gel-type electrode, the soft and dry nanomembrane electrode does not cause skin irritation even if it was used for a long-term<sup>32</sup>. To validate this point, we conducted the skin test by wearing the skin-like EMG sensor and the commercial sensor all day long (**Figure S5**). While the dry nanomembrane electrode in this work did not cause any skin irritation, the commercial gel-type electrode left a skin rash due to the inflammatory reaction. In addition to the inflammation-free nature of the skin-like EMG sensor, the device makes conformal contact with the deformable skin surface and thus minimizes the motion artifact mainly due to the serpentine electrode design and compact, flexible wireless circuit. The computational finite element analysis (FEA) in **Figure 3c** delineates the readily deformable mechanics of the serpentine nanomembrane. The graphical representation of FEA shows the von Mises stress distribution of the serpentine electrode under 30% of strain, and it suggests that the stress concentration at the inner circle of the serpentine design enables the electrode to stretch under strain<sup>33</sup>. The experimental study in **Figure 3d** corroborates the stretchable mechanics of the electrode, and the result indicates that the normalized resistance remained stable with a slight gradual increase even after 300 stretching cycles under 30% of strain. Besides the serpentine electrode, the flexible PCB used in this work transmitted steady wireless EMG voltage signals after hundreds of bending cycles despite the presence of the rigid microchips on the board as in **Figure S6**. In this regard, the high stretchability of the serpentine nanomembrane and flexibility of the circuit with miniaturized form factor make a synergistic contribution to the high skin-conformality of the device as it makes intimate contact with the irregular geometry of the various human body surfaces (**Figure S7**). **Figure 3e** depicts the circuit design of the flexible PCB that enables real-time data acquisition of the EMG signals as well as the wireless data transfer to the cloud, thereby eliminating the need for complicated wiring during EMG monitoring. Despite the

exceptional strengths of the skin-like EMG sensor, for the device in this work to be widely utilized in real-life studies, it should demonstrate comparable performance to the commercial EMG sensor. Hence, we collected the EMG signals with the EMG sensor in this work and the commercial sensor (BioRadio) during repeated elbow flexions. **Figure 3f** explicitly captures a highly equivalent performance of our device because the EMG signals acquired by both devices completely overlap with one another. Besides, as **Figure 3g** indicates, the signal-to-noise ratio (SNR) value of the commercial device was only 11% higher than that of the skin-like EMG sensor. The sensory technology developed in this work demonstrates that it can collect as accurate EMG signals as the commercial device without motion artifact and skin inflammation, thereby verifying its potential to construct the reliable sensory feedback loop that delivers the high-fidelity input for deep-learned motion classifications.

**Figure 4a** clarifies how the intent-driven exoskeleton operates based on the flow chart which is mainly comprised of three sections: EMG sensing artificial skin, cloud computing, and wearable robotic exoskeleton. It begins with the onset of muscle contraction during an arbitrary upper-limb movement by the user, and the multichannel sensors detect the EMG signals and wirelessly transmit the data to the cloud which conducts real-time signal processing and motion prediction. Signal processing segments the raw EMG signals into 1.0-second-long signals and applies a band-pass filter before rectifying the EMG data. Afterward, the deep-learning model based on the convolutional neural network (CNN) and long short-term memory (LSTM) predicts the motion class, which is then wirelessly transmitted to the exoskeleton unit (the detailed information about the deep-learning model is described in the Method section). Based on the predicted motion, the PAMs contract, and the displacement produced by PAM is then translated to the exoskeleton via cables such that the exoskeleton can assist the intended movement of the user in real-time. As shown in **Figure 4b**, four skin-like EMG sensors are attached to upper body muscles to collect the EMG signals of the biceps, triceps, medial deltoid, and latissimus dorsi since these muscles are responsible for target upper-limb movements in this work. **Figure 4c** portrays the collected EMG signals when the human subject advertently contracted the corresponding muscle. All graphs show a substantially decreased amplitude of EMG signals during rest, which is followed by explosive EMG activities during muscle contractions. In this work, we use the onset signals of muscle activation to determine the intended movement of the user in order to assist the movement of the user instantaneously. We devised the logic flow as in **Figure 4d** to classify and augment four different upper-limb movements in real-time. Starting with the ready state, the intent-driven exoskeleton distinguishes whether the biceps or medial deltoid are activated based on the EMG signals. When the skin-like EMG sensor detects the onset signal of the biceps, the exoskeleton starts pumping the PAM that augments elbow flexion, and the user can choose to pause or continue the movement using the triceps muscle. Thus, if the user activates the triceps muscle, the exoskeleton will pause and return to the rest position by venting the biceps PAM in the presence of additional triceps activation. We introduced this algorithm function because the user might intend to stop moving or want a partial movement instead of a full range of motion. In real-life situations, we do not always use the full range of motions for everyday tasks or even cease to move in the course of the movement. Otherwise, in the absence of triceps intervention, the exoskeleton keeps augmenting the elbow flexion. The same pattern applies for shoulder flexion except that the antagonistic muscle is latissimus dorsi in this case. Therefore, the exoskeleton will begin to pump the shoulder PAM when the skin-like EMG sensor detects the onset EMG signal of the medial deltoid. Just as with elbow flexion, the shoulder flexion will cease under the latissimus dorsi activation and return to the rest position if there are additional activation signals. Likewise, the exoskeleton will continue shoulder flexion in the absence of latissimus

dorsi muscle intervention. Furthermore, we can also combine two upper-limb movements to perform a more complex movement. For example, if the user pauses during elbow flexion by triceps activation and then activates the medial deltoid muscle, the exoskeleton will augment shoulder flexion, and the same posture can be attained in the reversed order (see dashed arrows in **Figure 4d**). The combination of upper-limb joint movements makes the exoskeleton much more functional because it allows multiple movements that can be utilized to conduct daily tasks. **Figure S8** exhibits the screenshot images of the cloud-based graphic user interface (GUI) that we developed for motion training and informative purposes. The GUI offers the cloud-user interface in a way that the user receives visual information about the current status, and it also allows the user to control each PAM manually. As illustrated in the first image, the GUI shows whether all the skin-like EMG sensors and the PAM controlling circuit in the backpack are connected to the cloud. The second image shows the interface during the real-time motion classification, in which the user can see the augmented motion and air pressure for each PAM. The last screenshot depicts the EMG monitoring during the motion training session. Here, the user can pause the ongoing movement assistance of the exoskeleton robot in case of emergency, and the individual PAM can be manually controlled simply by moving the three dots on the GUI in the top right corner.

**Figure 5a** illustrates the deep learning architecture of each muscle model designed for the classification of muscle activation in our study. The CNN+LSTM model proposed in this work receives epoch-by-epoch 1-second-long filtered EMG signals as inputs, which are then directed to one of the four single models depending on the location of the attached sensor. The individual models serve to classify muscle activation, and their outputs are aggregated to determine the necessary motion activation. **Supplementary Tables 2, 3, 4, and 5** elaborate on the details of the machine learning layer employed for four muscle activation classifications. To start with, we normalized the filtered EMG signals using the Standard Scaler method to convert them to values ranging from 0 to 1 and then employed the non-linear activation functions called Leaky Rectified Linear Units (Leaky ReLU). To optimize the CNN architecture, we used ADAM optimization with a learning rate of 0.0001 and utilized the cross-entropy loss function to calculate the error. During optimization, the batch size was set as 20, and a dropout deactivation rate of 0.3 was utilized to avoid overfitting. Early stopping was also used to prevent overfitting by randomly selecting 20% of the data from the training set and using it as a validation set at the beginning of the optimization phase. We conducted learning rate annealing with a factor of 5 once the validation loss stopped improving, and we utilized two one-dimensional convolutional layers in the CNN+LSTM model along with four units in the LSTM layers. A single convolutional cell (Conv\_1D) includes two convolutional layers, a layer of batch normalization, a Max pooling step layer with a filter size of 4, and a Leaky ReLU function layer. After the data was flattened, it was followed by fully connected layers and passed through a softmax layer to compute the predicted three classes (rest, on-set, activation). Through the random selection method, we optimized hyper-parameters, and the training was stopped when two successive decays occurred with no improvement in the network performance on the validation set. We constructed the model architecture based on our previous deep-learning models after major modifications such that it serves for the motion prediction scenario<sup>34, 35</sup>.

**Figure 5b** demonstrates real-time upper-limb movement augmentation for four target movements enabled by the intent-driven exoskeleton as a result of the deep learning model architecture that was discussed earlier. For all motions, if the user attempts to perform an arbitrary target motion and activates the corresponding muscle in charge, the exoskeleton detects the onset of the generated EMG signals and instantaneously assists the intended movement of the user right after the muscle activation. For instance, if the user at the rest

position tries to conduct elbow flexion, the cloud-based deep learning algorithm classifies the motion, and the exoskeleton starts to assist the elbow flexion in real-time as in Motion 1 of the figure. For Motion 2, the human subject at the rest position activates the triceps muscle, and the embedded deep learning algorithm determines the intended movement is the elbow extension, which is then assisted by the robot within a few milliseconds. The same applies to Motion 3 and 4, which deal with joint shoulder movements. Hence, in Motion 3, when the wearer at the rest position attempts to activate the medial deltoid, the exoskeleton quickly captures the intention of the user and augments the shoulder flexion. Lastly, the exoskeleton assists the shoulder extension when the user activates the latissimus dorsi as in Motion 4. **Video S1** also shows the exoskeleton that assists all the upper-limb movements in a continuous real-time sequence along with the GUI screen. In brief, all the user needs to do for strength assistance is to conduct any of the trained upper-limb movements because the system is completely intent-driven. Until now, there has not been any type of work that successfully delivered a fully functional intent-driven prototype with total integration of sensory feedback, strength augmentation, and a human intention predicting algorithm in a way that assists four upper limb movements based on the user's intention in real-time. The CNN+LSTM model developed in this work can classify muscle activation based on filtered EMG signals, and we evaluated its performance using a confusion matrix. For the model architecture, we obtained 50 sets of EMG data for each movement data from five human subjects, of which we used 80% of the obtained EMG data for training and the other 20% of data to construct and validate the deep-learning model. As depicted in **Figure 5c**, the model achieved a high test accuracy of 95.38% for biceps/triceps muscle activation classification and 97.01% for medial deltoid/latissimus dorsi muscle activation classification. The high accuracy (96.2%, on average) achieved in this work corroborates the reliability of the model and suggests that the exoskeleton will assist the joint movement just as intended with minimized errors. The cloud returns motion classes with a 200-250 ms response rate to the tablet in real-time for exoskeleton driver actuation, and if we consider the delay for PAM actuation, the overall movement assistance takes 300-350 ms, which is fast enough to support the joint movement. We expect that the deep-learning model in this work can also be directly implemented in the development of advanced prosthetics or assistive devices that can respond to changes in muscle activation in real-time.

To examine the quantitative strength augmentation that the intent-driven exoskeleton can provide, we compared the EMG signals when performing the trained upper-extremity joint movements with and without exoskeletons as in **Figures 6a** and **b**. **Figure 6a** demonstrates the filtered EMG signals that were generated as the human subject repeated elbow flexion with and without the exoskeleton. The result substantiates a tremendous strength augmenting effect of the exoskeleton because the average EMG activation amplitude of the biceps with the exoskeleton was 6.9 times lower than that without the exoskeleton during elbow flexion. Similarly, the EMG signals of the medial deltoid exhibited a substantial difference when the exoskeleton augmented the shoulder flexion (**Figure 6b**). The inset figure implies that the average EMG signal amplitude was 3.4 times lower with the assistance of the exoskeleton robot, underlining the high force and displacement generation capability of the PAM to assist the upper-extremity movements. These differences demonstrated that the exoskeleton can augment the upper-extremity movements by 5.15 times, on average. In addition to the strength assistance without any mechanical load, **Figure 6c** shows strength augmentation even with a moderately heavy load. The human subject was asked to conduct elbow flexion and shoulder flexion while holding the 6.8 kg (15 lb) dumbbell. The result shows that the exoskeleton reduced the EMG activities by 1.7 fold and 2.1 fold for elbow flexion and shoulder flexion respectively (**Figure S9**), indicating that the exoskeleton can still augment human strength even when holding

considerably heavy objects. In addition to assisting dynamic joint movements, the exoskeleton can help the human subject hold the weight against gravity in a static manner for an extended period of time. For instance, in **Video S2**, the human subject was then asked to keep holding the 6.8 kg weight with and without the assistance of the exoskeleton. While the human subject with the assistance could lift the weight without much difficulty for longer than 3 minutes, the same human subject could not proceed longer than one minute without the assistance of the exoskeleton. **Figure 6d** demonstrates the real-life usage examples of the exoskeleton to assist the movement for completing daily tasks. Since the exoskeleton in this work can support a variety of upper-limb joint movements including the combined movement of shoulder flexion and elbow flexion, it can assist in completing several daily tasks such as placing a box, drilling, reaching out for a doorknob, and getting up from a chair with the arm support as in **Figure 6d** and **Video S3**. Lastly, the cloud-computing platform in this work enables the system to collect a massive amount of training data from multiple users who use other local devices with the global data cloud server, and it also allows us to update the deep-learning model simultaneously to further enhance the classification accuracy. Thus, future work in this study will include establishing the universal, generalized deep-learning model that accurately predicts the intended movement of multiple human subjects, instead of just a single person, such that it can serve to augment the strength of a large mass of human subjects as it is illustrated in **Figure S10**. In this regard, the cloud-computing platform that is integrated with the soft bioelectronics and human strength augmenting exoskeleton will not only lay a fundamental groundwork for our future work but also make a substantial contribution to a variety of next-generation human-robot interaction studies.

## Discussion

In summary, this study delivers the total integration of a motion-predicting cloud computing platform, a robotic exoskeleton for strength augmentation, and soft bioelectronics-enabled sensory feedback to develop the fully-intent driven robotic exoskeleton that assists the human upper-extremity joint movements. The PAM module can provide a maximum power source of 895 N of force and 87 mm of displacement that is translated to the exoskeleton frame such that the multiple upper-extremity joint movements can be augmented while retaining a lightweight structure. The skin-like bioelectronics enables sensory feedback by monitoring the EMG signals, which are processed through cloud computing to predict the intended movement of the user. The cloud-based deep-learning algorithm can classify four upper-extremity movements in total with a high test accuracy of 95.4% and 97.0% for biceps/triceps and medial deltoid/latissimus dorsi movements respectively. The overall response time for the movement assistance, which includes the EMG onset signal detection, cloud-based motion prediction, and actuation, consumes approximately 300-350 ms. Moreover, owing to the high force and displacement generation capability of PAM units, the intent-driven exoskeleton augments the upper-extremity strength substantially as it reduced the EMG activities by 6.9 and 3.4 times during elbow and shoulder flexion respectively. In addition, the exoskeleton also assisted the loaded movements by 1.7 and 2.1 times for elbow and shoulder flexion respectively, demonstrating that it can be used to carry or move moderately heavy objects in daily life. Until now, there has been no work that seamlessly integrated all the cutting-edge technologies into an intent-driven, fully working robotic exoskeleton that can be directly employed in real-life situations. In this context, we expect that the intent-driven exoskeleton in this study will not only make a significant contribution to next-generation robotics technology but it will also have a transformative impact on the lifestyle of individuals with neuromotor disorders.

## Methods

**PAM fabrication and characterization.** The actuator consists of a bladder made of 3/4" silicone tubing (51135K45, McMaster), a 1 1/4" polyester mesh expandable sleeving (2837K77, McMaster), two custom machined 6061-T6 aluminum end fittings, two 3/4" stainless steel PEX-B pinch clamps (Home Depot) and a 1/4" push to connect fitting (5779K494, McMaster).

To characterize the PAM, the quasistatic testing of the PAMs was performed with a Mark-10 ESM303 1.5 kN motorized test stand with a Mark-10 Series 5 1 kN force meter (M5-200). The test procedure involved a blocked-force test where the PAMs were held at maximum length and then pressurized. This was followed by programming the motorized test stand to perform a slow unloading and loading ramp at 100 mm min<sup>-1</sup>, where the PAM was allowed to contract until zero force and then stretched back to maximum length. Force and length data were recorded for 10-80 psi in steps of 10 psi.

**Exoskeleton fabrication and integration with the PAM module.** To make the exoskeleton firm, stiff, and lightweight, it was mostly made of carbon fiber with machined aluminum connectors and stainless steel fasteners. The super swivel ball joint (6960T23, McMaster) that connects the exoskeleton to the backpack enables it to move naturally with the body. The main vertical strut between the hip and shoulder joint and the strut between the shoulder and elbow joints were built using two telescoping collet sets (Dragon Plate), 0.5" and 0.625" ID carbon fiber twill weave telescoping tubing. This technique makes it simple to adapt the exoskeleton to various subject body sizes since the lengths from the hip to the shoulder, the shoulder to the elbow, and the elbow to the wrist can all be quickly altered. Fitment problems may arise while attempting to create a comfortable interaction between the exoskeleton and the user. However, by utilizing 3D printing for the upper and lower arm mounts, both universal and custom arm mounts can be quickly created and attached to the exoskeleton. The arm mounts in this design are ergonomically attached to the curved geometry of the arm by being hot water thermoformed after being 3D printed as a flat shape. An inline ball joint (8412K12, McMaster) connects the carbon fiber tubing to the 3D-printed upper arm mount to increase arm movement. As shown in **Figure S11**, 3 mm and 4 mm carbon fiber plates (generic 3K carbon fiber plate, Amazon) are used to construct the shoulder joint. The plate carbon fiber is cut to the appropriate shape using a waterjet, and the plates are sanded and epoxied together (Scotch-Weld™ DP-2216, 3M) to form the joint geometry. A similar manufacturing process is used for the elbow joint. The interface between the telescoping tubing and the joints is machined aluminum and epoxied into the telescoping tubing. To provide smooth joint motions, a standard 605 bearing with an aluminum press-fit housing is bolted into carbon fiber.

**Skin-like EMG sensor fabrication.** The fabrication process of the proposed system involved three main steps, including fabric substrate fabrication, circuits and encapsulation fabrication, nanomembrane electrode fabrication, and overall assembly. Fabric substrate fabrication involved mixing Silbione (A-4717, Factor II Inc.) parts A and B in a 1:1 weight ratio for ten minutes. The mixed uncured Silbione was then spin-coated on a polytetrafluoroethylene (PTFE) sheet at 1200 RPM for one minute to ensure uniform adhesion layer thickness. The surface was covered with brown fabric medical tape (9907T, 3M) and subjected to curing in an oven at 65°C for 30 minutes. The PTFE sheet was then detached after the Silbione was cured. In the fabrication of circuits and encapsulation, we used a flexible PCB (fPCB) and mounted all electronic components on it with a reflow solder process (**Figure S3**). Laser cutting was performed to remove unnecessary areas to enhance the mechanical flexibility of the circuit. For power supply and management, we utilized a lithium polymer battery assembly with a slide switch and a circular magnetic recharging port. A low-modulus elastomer (Ecoflex Gel, Smooth-On) was placed underneath the integrated circuit to isolate the strain. The entire electronic system was encapsulated and soft-packaged with an additional elastomer (Ecoflex

00-30, Smooth-On), with only the switch and charging port exposed. The nanomembrane electrode fabrication process involved utilizing gold/chromium electrodes (thickness: 200 nm for Au and 25 nm for Cr), which were deposited by E-beam evaporation and facile laser cutting. PDMS (Sylgard 184, Dow) was employed as the bottom layer of the electrode fabrication due to its proper adhesion and easy-release features. A polymer film (18-0.3F, CS Hyde) was laminated onto the cured PDMS surface, and gold was deposited on the film using an electron-beam deposition process. The film was then laser ablated to obtain a stretchable serpentine pattern of the electrode. Non-functional materials besides the electrode patterns were removed by delaminating them from the PDMS surface with a tweezer. For the final assembly of the electrode system and fabric substrate, gold electrodes were transferred to the fabric's soft adhesive side using water-soluble tape (ASW-35/R-9, Aquasol Corporation). The electrode system-mounted fabric was then patterned using a laser cutting process, and the soft-packaged electronic system was attached to the fabric side of the fabric substrate by adding and curing a thin layer of silicone.

**Skin-like EMG sensor characterization.** The experimental setup for the mechanical and electrical tests consisted of a digital force gauge (M5-5, Mark-10) and a motorized test stand (ESM303, Mark-10) for measuring mechanical properties, and an LCR meter (Model 891, BK Precision) for measuring electrical resistance. For the cyclic stretching test, the electrode system was stretched and relaxed vertically with a speed of 100 mm/min for 300 cycles, while for the circuit bending test, the system was repeatedly stretched and relaxed at the same speed for 400 cycles. The EMG voltage signal was recorded using a custom android software application (Bio-monitor) during the test. To compare the skin impedance of the electrode, the gold electrode was transferred to the brown tape with the adhesive on it (1200 RPM spin-coated Silbione, Ecoflex 00-30, PDMS). A control group experiment was also conducted with a gel electrode to compare electrode-skin contact impedance. The test was conducted on the biceps, and the electrode attached area was cleaned with a skin preparation gel (NuPrep Skin Prep Gel, Weaver & Co.). The electrode-skin contact impedance was measured by a skin impedance meter (Model 1089NP Checktrode, UFI) connected to two electrodes on the skin. For the signal-to-noise ratio (SNR) calculation of the data, the noise was assumed to be the data measured before elbow flexion without any activity, and its amplitude was computed. The SNR value was calculated using the following equation:  $SNR_{dB} = 20 \log_{10} \left( \frac{A_{Signal}}{A_{Noise}} \right)$  Finally, the finite element analysis (FEA) study focused on the mechanical reliability of the two-layered electrode (gold and polyimide) when applied for the yield of 30% strain. We used commercial finite element analysis software (Abaqus, Dassault Systemes Simulia Corporation, Johnston, RI) for simulation and plotted strain distributions with the system on human skin. The simulation used the following material properties: Young's modulus (E) and Poisson's ratio ( $\nu$ ): E (PI) = 2.5 MPa and  $\nu$  (PI) = 0.34 for PI, E (au) = 78 MPa,  $\nu$  (au) = 0.44 for Au.

**Data processing and acquisition.** All data processing was done with Python and the data measured with our system was first processed by a bandpass filter and notch filter. The cut-off frequencies of the bandpass filter used were 10-250Hz for EMG. The stop band frequency of the notch filter was set to 59-61 Hz to remove the power line noise at 60 Hz. During the first stage of EMG acquisition, an instrumentation amplifier (IA) was utilized to amplify the voltage differential between each channel. To prevent electrode DC offset from causing IA saturation, the IA gain was set appropriately. Moreover, the high common mode rejection ratio (CMRR) of the IA reduced the common mode voltage required by the user. A negative feedback circuit utilizing a reference electrode was employed to reduce common mode voltages, which is a popular method for capturing biopotentials. The second stage employed a band-pass filter (BPF) that consists of a low-pass filter and a high-pass filter. The second-order high-pass filter

eliminated lower-frequency noise caused by electrode positioning, skin-electrode contact, and other movements. After removing the DC component, the signal was amplified once more, and a potentiometer was used to supply bias voltage to the amplifiers, resulting in a positive output voltage that was adjusted to match the analog-to-digital converter's input signal.

**Data cloud computing interface and firmware development.** The circuit used for wireless recording of non-invasive electromyogram (EMG) signals on the biceps brachii, triceps brachii, and medial deltoid muscles include a microcontroller (nRF52832, Nordic Semiconductor) and a Bluetooth system-on-chip with an analog front-end (ADS1292, Texas Instruments). The ADS1292 IC component and hardware structure are used to organize the analog-to-digital converter (ADC) operation and digital data encoding for Bluetooth buffer transfer. The digital signal with a 10-bit ADC is transmitted with the ADC output's decimal value representing the minimum to maximum muscle movement range. The microcontroller nRF52832 wirelessly transmits data to the mobile device (tablet, Galaxy Tab S8, Samsung) via Bluetooth low energy (BLE). The device is powered by a 40 mAh rechargeable lithium-polymer battery, which has a battery life of approximately 5.1 hours after a full charge. The EMG data from multiple muscle locations are recorded and sent to Google Cloud using a custom Android app on a Galaxy Tab S8 tablet. Cloud computing is used for real-time motion applications due to computing power and processing limitations. The cloud software architecture includes a mobile application that connects captured sensors to cloud data storage, where the machine learning algorithm is hosted. The cloud software preprocesses the data and sends it to a CNN + LSTM algorithm that was developed using the Keres library in Python with other libraries for matrix operations. The cloud returns motion classes with a 200-250 ms response rate to the tablet in real-time for exoskeleton driver actuation. The exoskeleton driver uses a microcontroller (nRF52832, Nordic Semiconductor), internal and external pressure feedback system, and valve control GPIOs. The pressure system provides pressure feedback to the entire system for valve and compressor control. The valve control works with multiple GPIO of the microcontroller, with a response time of 50 ms. The user's onset and specific muscle motion signals, classified from the cloud, actuate the robotic exoskeleton for user strength augmentation.

**Deep-learning motion classifications.** A CNN+LSTM model was utilized in this study using TensorFlow in Python on a laptop equipped with an Intel i7 processor (I7-9750H). The 1-second segmented EMG signals were divided into three parts for model training: 60% for training, 20% for validation, and 20% for testing. The CNN network parameter weight was updated during each training step based on the model training validation accuracy. Hyperparameter values, such as learning rate, kernel size, a filter of each convolutional layer, and the unit of each dropout, were selected using a random search method. The model with the highest validation accuracy was chosen as the best model. To evaluate its performance, the test dataset was used to determine the prediction accuracy of the best model. The study used filtered EMG signals that were normalized using the standard scaler method and Leaky ReLU activation functions. ADAM optimization was used with a learning rate of 0.0001 and the cross-entropy loss function. The batch size was set to 20, and a dropout deactivation rate of 0.3 was utilized to prevent overfitting. Early stopping was also employed with a validation set. The CNN+LSTM model included two one-dimensional convolutional layers, two convolutional cells, and fully connected layers that predicted three classes. **Tables S2, 3, 4, and 5** contain more detailed information about the deep-learning model.

**Strength augmentation demonstration.** To evaluate the effectiveness of the exoskeleton, the EMG signals collected during the experiment were analyzed. Specifically, the average EMG signal amplitude was calculated to quantify the level of muscle activation. The comparison of average EMG signal amplitude between the two conditions (with and without exoskeleton assistance) determined the strength augmentation provided by the exoskeleton. Additionally,



the results were compared between the two versions of the exoskeleton (with and without a 10lb dumbbell) to evaluate the impact of the added weight on the effectiveness of the exoskeleton.

### **Data Availability**

All data supporting the findings of this study are available upon reasonable request from the corresponding author.

### **Code Availability**

All code used to generate the results in this paper is available upon reasonable request from the corresponding author.

### **Acknowledgments**

The authors acknowledge the support from the SEMI-FlexTech and the IEN Center for Human-Centric Interfaces and Engineering at Georgia Tech. This material is based on research sponsored by Army Research Laboratory under Agreement Number W911NF-19-2-0345. The U.S. Government is authorized to reproduce and distribute reprints for Government purposes notwithstanding any copyright notation thereon. The views and conclusions contained herein are those of the authors and should not be interpreted as necessarily representing the official policies or endorsements, either expressed or implied, of the Army Research Laboratory (ARL) or the U.S. Government.

### **Author contributions**

J.L., K.K., I.S., and W.-H.Y. designed the research project; J.L., K.K., I.S., J.M., Y.L., H.K., L.R., N.Z., Y.K., S.K., J.L., Y.N., S.L., F.H., M.S., and W.-H.Y. performed research; J.L., K.K., I.S., and W.-H.Y. analyzed data; and J.L., K.K., and W.-H.Y. wrote the paper.

### **Competing interests**

Georgia Tech has a pending US patent application regarding the materials in this paper.

### **References**

1. in Why stroke matters, Vol. 2022 Facts and Figures about Stroke (World Stroke Organization, 2023).
2. Li, S. Spasticity, motor recovery, and neural plasticity after stroke. *Frontiers in neurology* **8**, 120 (2017).
3. Demaerschalk, B.M., Hwang, H.-M. & Leung, G. US cost burden of ischemic stroke: a systematic literature review. *The American journal of managed care* **16**, 525-533 (2010).
4. Irshaidat, M., Soufian, M., Al-Ibadi, A. & Nefti-Meziani, S. in 2019 2nd IEEE international conference on soft robotics (RoboSoft) 630-635 (IEEE, 2019).
5. Ang, B.W. & Yeow, C.-H. Design and modeling of a high force soft actuator for assisted elbow flexion. *IEEE Robotics and Automation Letters* **5**, 3731-3736 (2020).
6. Das, S. & Kurita, Y. ForceArm: a wearable pneumatic gel muscle (PGM)-based assistive suit for the upper limb. *IEEE Transactions on Medical Robotics and Bionics* **2**, 269-281 (2020).
7. Lotti, N. et al. Adaptive model-based myoelectric control for a soft wearable arm exosuit: A new generation of wearable robot control. *IEEE Robotics & Automation Magazine* **27**, 43-

53 (2020).

8. Nassour, J., Zhao, G. & Grimmer, M. Soft pneumatic elbow exoskeleton reduces the muscle activity, metabolic cost and fatigue during holding and carrying of loads. *Scientific Reports* **11**, 1-14 (2021).
9. Samper-Escudero, J.L., Coloma, S., Olivares-Mendez, M.A., González, M.Á.S.-U. & Ferre, M. A compact and portable exoskeleton for shoulder and elbow assistance for workers and prospective use in space. *IEEE Transactions on Human-Machine Systems* (2022).
10. Babič, J., Petrič, T., Peternel, L. & Morimoto, J. in 2017 IEEE International Conference on Robotics and Automation (ICRA) 5929-5934 (IEEE, 2017).
11. Samper-Escudero, J.L., Giménez-Fernandez, A., Sánchez-Urán, M.Á. & Ferre, M. A cable-driven exosuit for upper limb flexion based on fibres compliance. *IEEE Access* **8**, 153297-153310 (2020).
12. Kim, Y.G. et al. A voice activated bi-articular exosuit for upper limb assistance during lifting tasks. *Robotics and Computer-Integrated Manufacturing* **66**, 101995 (2020).
13. Proietti, T. et al. Sensing and control of a multi-joint soft wearable robot for upper-limb assistance and rehabilitation. *IEEE Robotics and Automation Letters* **6**, 2381-2388 (2021).
14. Missiroli, F. et al. Rigid, soft, passive, and active: A hybrid occupational exoskeleton for bimanual multijoint assistance. *IEEE Robotics and Automation Letters* **7**, 2557-2564 (2022).
15. Khan, A.M. et al. Estimation of desired motion intention and compliance control for upper limb assist exoskeleton. *International Journal of Control, Automation, and Systems* **15**, 802 (2017).
16. Liu, H., Tao, J., Lyu, P. & Tian, F. Human-robot cooperative control based on sEMG for the upper limb exoskeleton robot. *Robotics and Autonomous Systems* **125**, 103350 (2020).
17. McDonald, C.G., Dennis, T.A. & O'Malley, M.K. in 2017 international conference on rehabilitation robotics (ICORR) 164-169 (IEEE, 2017).
18. Zhou, Y. et al. in 2021 27th International Conference on Mechatronics and Machine Vision in Practice (M2VIP) 498-503 (IEEE, 2021).
19. Georgarakis, A.-M., Xiloyannis, M., Wolf, P. & Riener, R. A textile exomuscle that assists the shoulder during functional movements for everyday life. *Nature Machine Intelligence* **4**, 574-582 (2022).
20. Shin, J.H. et al. Wearable EEG electronics for a Brain-AI Closed-Loop System to enhance autonomous machine decision-making. *npj Flexible Electronics* **6**, 32 (2022).
21. Mahmood, M. et al. Fully portable and wireless universal brain-machine interfaces enabled by flexible scalp electronics and deep learning algorithm. *Nature Machine Intelligence* **1**, 412-422 (2019).
22. Edelman, B.J. et al. Noninvasive neuroimaging enhances continuous neural tracking for robotic device control. *Science robotics* **4**, eaaw6844 (2019).
23. Dittmar, D., Dahlin, J., Persson, C. & Schuttelaar, M.-L. Allergic contact dermatitis caused by acrylic acid used in transcutaneous electrical nervous stimulation. *Contact Dermatitis* **77**,

409-412 (2017).

24. Hansel, K. et al. Contact sensitivity to electrocardiogram electrodes due to acrylic acid: A rare cause of medical device allergy. *Contact Dermatitis* **82**, 118-121 (2020).
25. Wu, H. et al. Materials, devices, and systems of on-skin electrodes for electrophysiological monitoring and human-machine interfaces. *Advanced Science* **8**, 2001938 (2021).
26. Kalita, B., Leonessa, A. & Dwivedy, S.K. in *Actuators*, Vol. 11 288 (MDPI, 2022).
27. Su, H. et al. in *Actuators*, Vol. 11 92 (MDPI, 2022).
28. Tiziani, L.O. & Hammond, F.L. Optical sensor-embedded pneumatic artificial muscle for position and force estimation. *Soft robotics* **7**, 462-477 (2020).
29. Riemann, B.L. & Lephart, S.M. The sensorimotor system, part I: the physiologic basis of functional joint stability. *Journal of athletic training* **37**, 71 (2002).
30. Ludewig, P.M. & Cook, T.M. Alterations in shoulder kinematics and associated muscle activity in people with symptoms of shoulder impingement. *Physical therapy* **80**, 276-291 (2000).
31. Chow, D.H. et al. The effect of backpack load on the gait of normal adolescent girls. *Ergonomics* **48**, 642-656 (2005).
32. Kim, H., Kim, E., Choi, C. & Yeo, W.-H. Advances in soft and dry electrodes for wearable health monitoring devices. *Micromachines* **13**, 629 (2022).
33. Zhang, Y. et al. Mechanics of ultra-stretchable self-similar serpentine interconnects. *Acta Materialia* **61**, 7816-7827 (2013).
34. Kwon, Y.-T. et al. All-printed nanomembrane wireless bioelectronics using a biocompatible solderable graphene for multimodal human-machine interfaces. *Nature communications* **11**, 3450 (2020).
35. Kwon, Y.-T. et al. Printed, wireless, soft bioelectronics and deep learning algorithm for smart human-machine interfaces. *ACS Applied Materials & Interfaces* **12**, 49398-49406 (2020).
36. Sabir, S.U.B., Ahmed, K., Sabir, U. & Naseer, N. in 2021 International Conference on Artificial Intelligence and Mechatronics Systems (AIMS) 1-6 (IEEE, 2021).
37. Wu, Q., Chen, B. & Wu, H. Neural-network-enhanced torque estimation control of a soft wearable exoskeleton for elbow assistance. *Mechatronics* **63**, 102279 (2019).
38. Dindorf, R. & Wos, P. Using the bioelectric signals to control of wearable orthosis of the elbow joint with bi-muscular pneumatic servo-drive. *Robotica* **38**, 804-818 (2020).

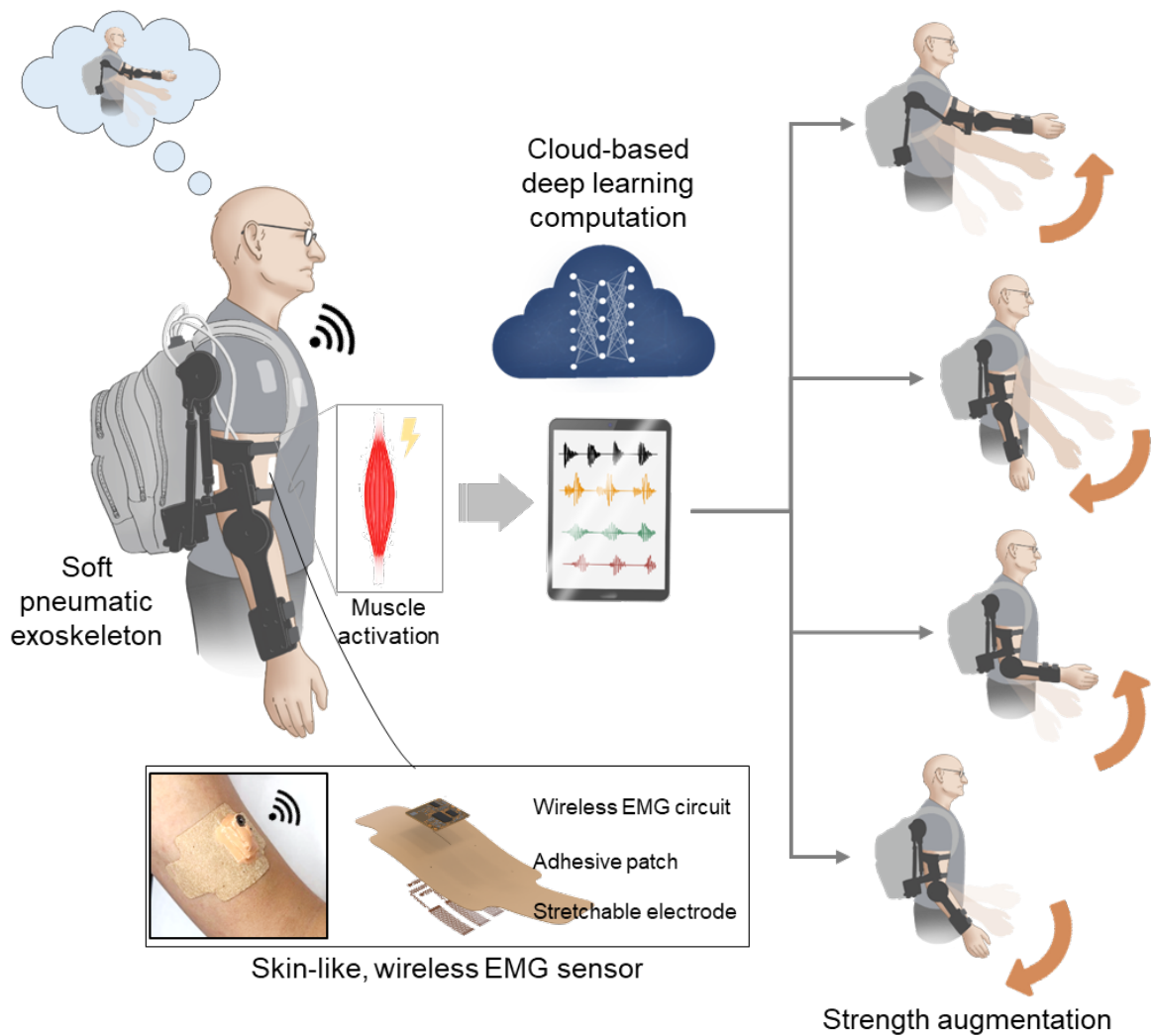


**Figure 1: Overview of seamless integration system of the soft pneumatic exoskeleton, skin-like EMG sensor, and cloud-based deep learning computation for intent-driven upper-limb strength augmentation.** The backpack contains three pneumatic artificial muscles (PAM) that operate just as the human muscles contract/relax to translate the generated force and displacement to the exoskeleton frame. The inset figure shows the snapshot of the skin-like, wireless EMG sensor attached to the biceps brachii and the exploded view of the skin-like sensor that consists of a wireless EMG circuit, biocompatible adhesive patch, and stretchable dry Au electrode.

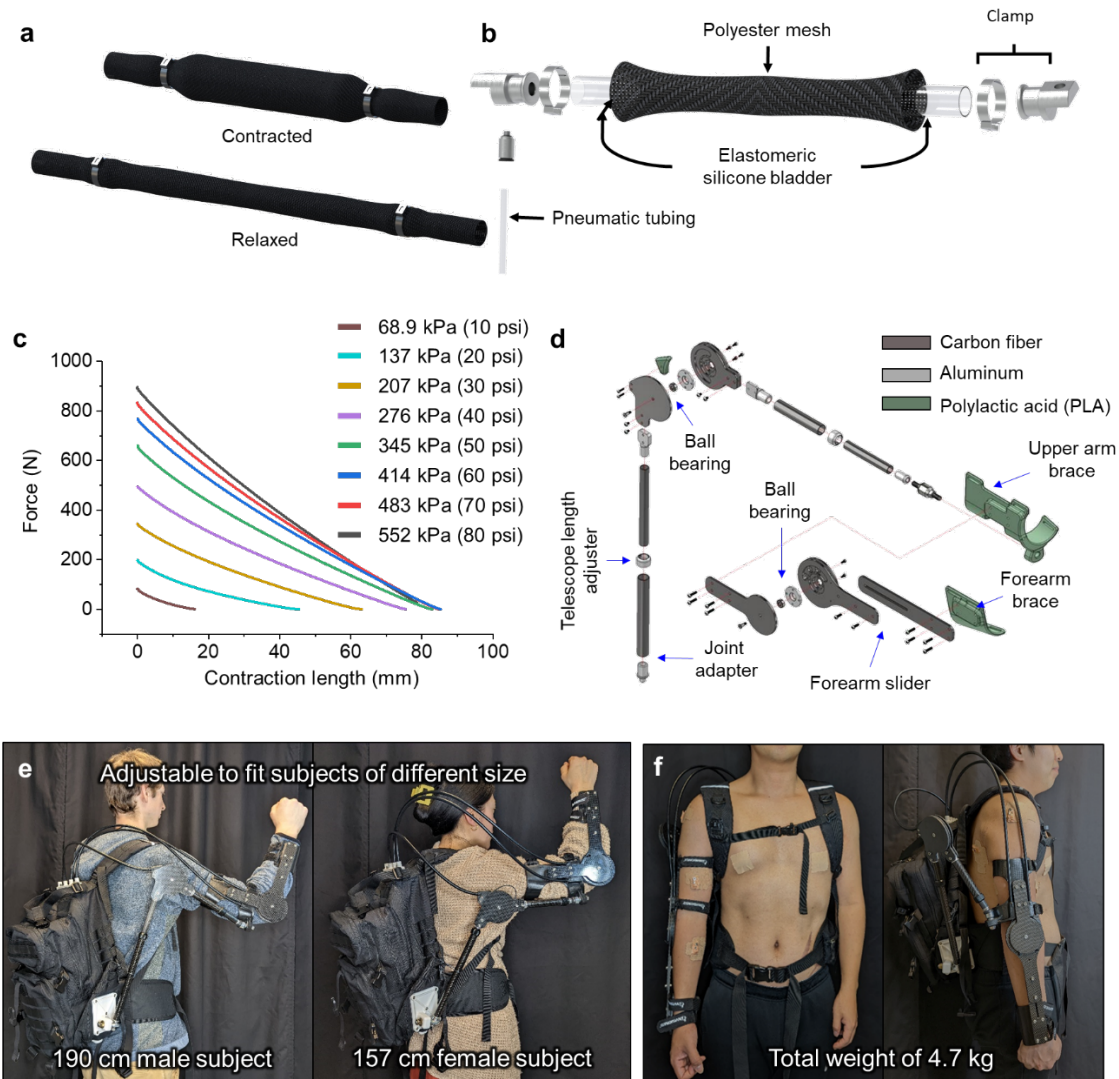


**Figure 2: Design and characterization of PAM and exoskeleton.** (a) Graphical illustration of the PAM in the contracted and relaxed states. (b) Exploded view of the PAM. (c) Relationship between force and contraction length as pressure increases from 68.9 kPa to 552 kPa. (d) Exploded view of the exoskeleton frame. (e) Snapshots of the 190 cm male subject and 157 cm female subject wearing the exoskeleton to capture the “one size fits all” design rationale. (f) Photograph of the human subject wearing the exoskeleton and skin-like EMG sensors.

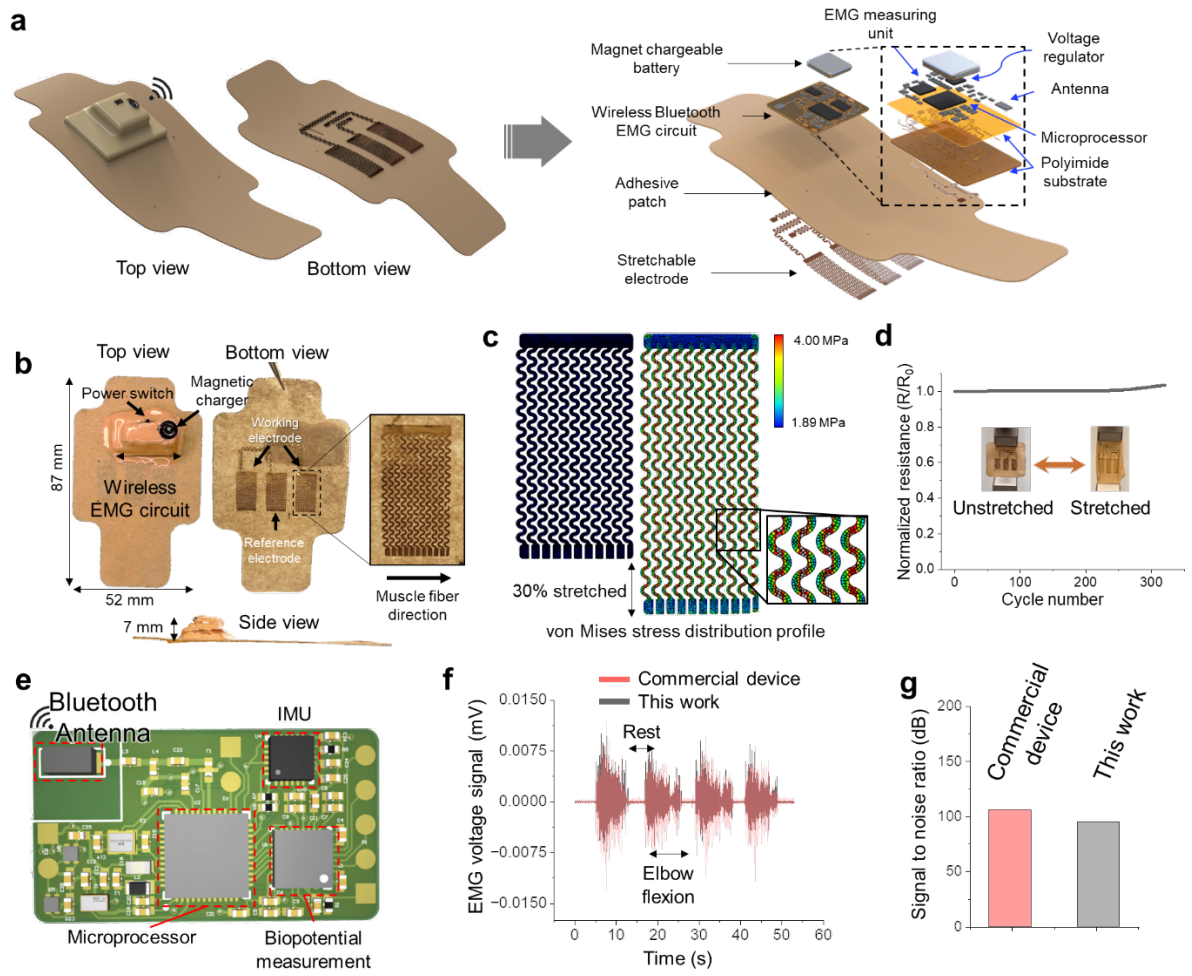


**Figure 3: Characterization of skin-like, wireless EMG sensor.** (a) Graphical illustration of the skin-like sensor and its exploded view. (b) Top, bottom, and side views of the skin-like EMG sensor. The flexible circuit consists of a customized magnet chargeable battery and power switch. (c) Finite element analysis of the stretchable electrode that is made up of polyimide and gold. The inset figure captures the magnified view of the von Mises stress distribution. (d) Cyclic stretching test of the stretchable electrode that is transferred to the adhesive patch. The strain applied to the electrode is 0.3 (e) Graphical illustration of the flexible circuit that consists of a wireless Bluetooth antenna, microprocessor, inertia measurement unit, and EMG measuring chip component. (f) EMG voltage signals that were measured with commercial and skin-like EMG sensors during intermittent elbow flexion movements. (g) Signal-to-noise ratio of the commercial and skin-like EMG sensors during elbow flexion.

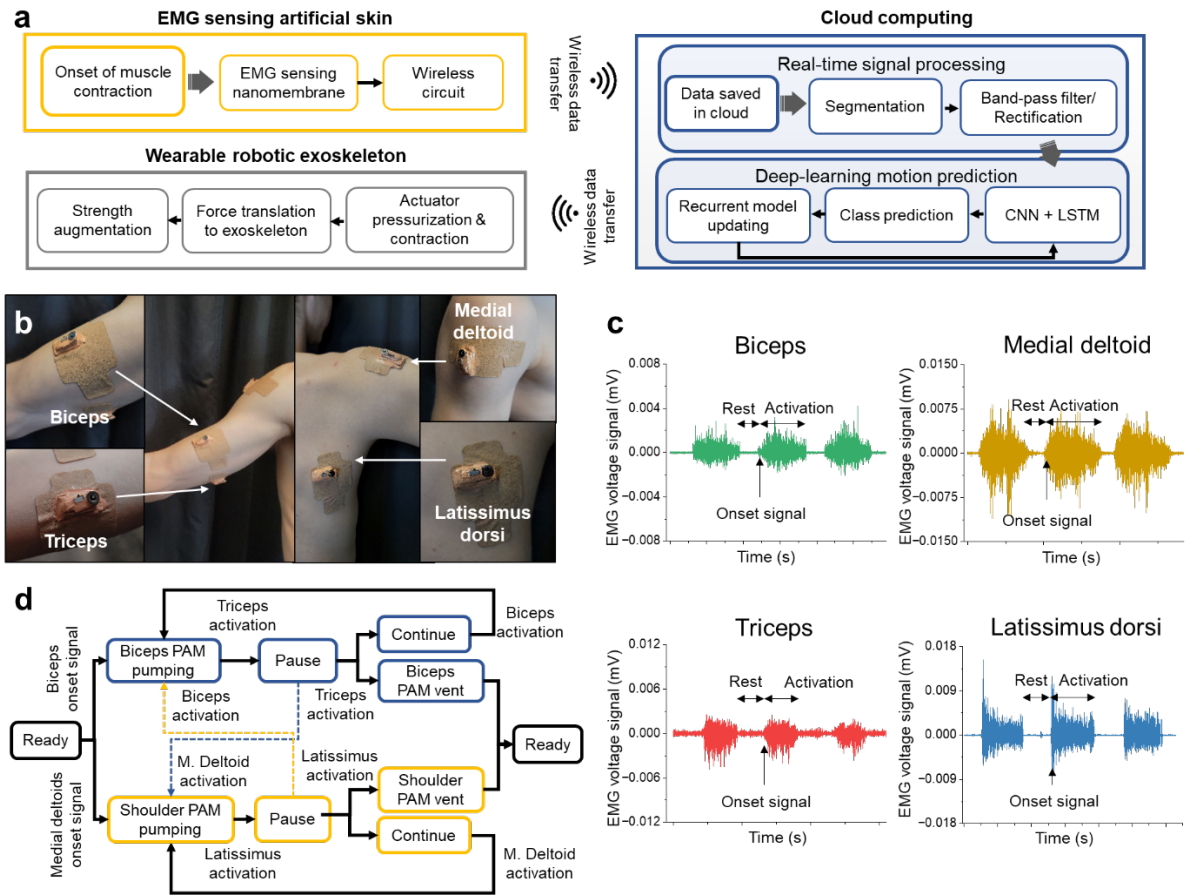


**Figure 4: Control and motion classifications of upper-limb joint movements.** (a) flow chart of the intent-driven exoskeleton with the flow from EMG sensing artificial skin, cloud computing, and then to the wearable robotic exoskeleton. (b) Skin-like EMG sensors mounted on the human subject's biceps brachii, triceps brachii, medial deltoid, and latissimus dorsi. (c) Signal-processed EMG signals of four different muscle parts during intermittent muscle activations. (d) Work logic flow of the upper-limb strength assistance based on sensory feedback, exoskeleton, and deep-learning algorithm for real-time joint movement classification.



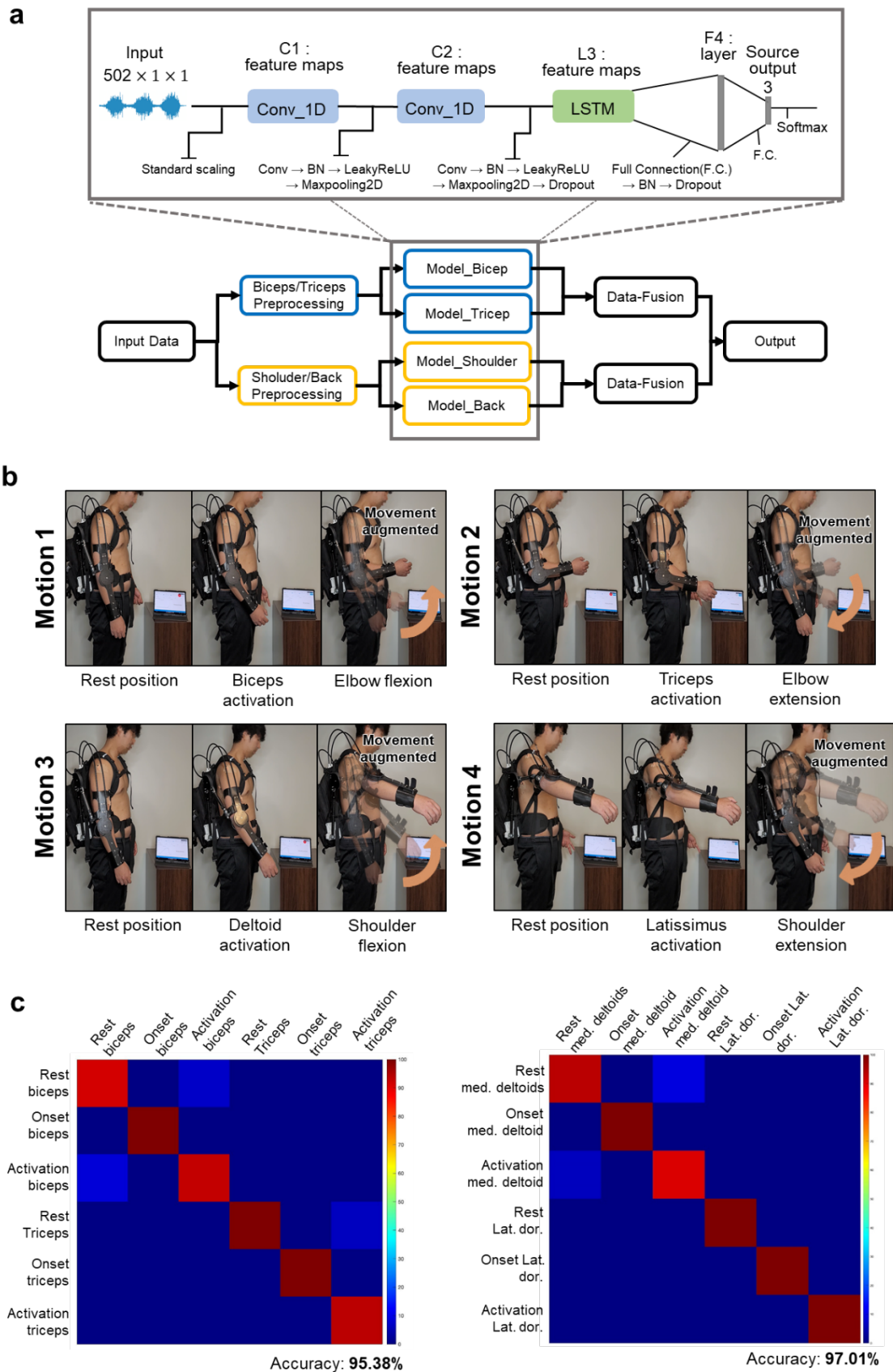


**Figure 5: Deep-learning model examination and integration into the intent-driven robotic**



**system.** (a) Model architecture of the cloud-based deep-learning algorithm. (b) Demonstration of four different joint movement augmentation in real-time in sequential order, which includes elbow flexion, elbow extension, shoulder flexion, and shoulder extension. (c) Confusion matrices that deliver the model classification accuracy of 95.38% and 97.01% for biceps/triceps and medial deltoid/latissimus dorsi respectively.

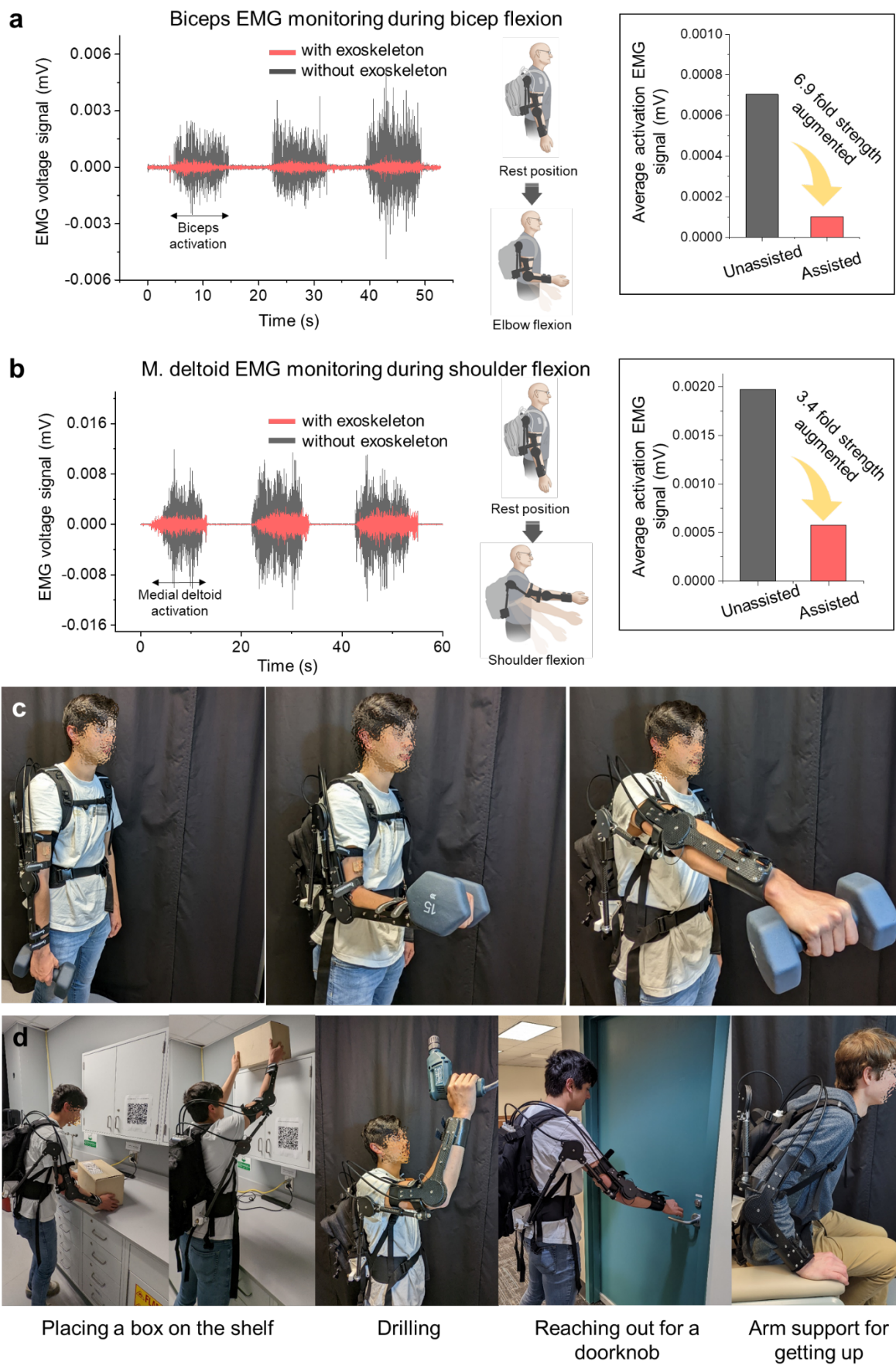


**Figure 6: Examining strength augmentation of joint movements and potential**

**applications in real life.** (a) Comparison of the EMG activities with and without the exoskeleton assistance during repeated elbow flexion. (b) Comparison of the EMG activities with and without the exoskeleton assistance during repeated shoulder flexion. The insets show in (a) and (b) the average activation EMG signal reduction when the exoskeleton assists the joint movements. (c) Investigation of the EMG activation reduction during elbow flexion and shoulder flexion while holding a 6.8 kg weight with the robot assistance. The exoskeleton assistance reduced the EMG activities by 1.7 fold and 2.1 fold. (d) Potential applications of the exoskeleton to assist practical daily life activities such as placing a box on the shelf/taking it back, drilling, reaching out for a doorknob, and getting up from a chair with the arm support.

**Table 1.** Comparison of this work with other upper extremity augmentation exoskeletons.

References	Integrated system*	Real-time prediction of human intention and constant model update		Human strength augmentation			Sensory feedback		
		real-time deep-learning	cloud computing	portable	motions	target movements	sensor configuration	sensor type	wireless
This work	O	O	Yes	O	4	Shoulder flexion/extension/elbow extension/ flexion	Skin-conformable	Dry electrode	O
36	O	O	X	O	3	Vertical shoulder flexion/elbow extension/flexion	Rigid	Commercial gel type	X
37	O	O	X	O	2	Elbow extension/ flexion	Rigid	Commercial gel type	X
16	O	O	X	X	2	Elbow extension/ flexion	Rigid	Commercial gel type	X
18	X	O	X	X	3	Shoulder abduction/ Vertical shoulder flexion/Horizontal flexion	Rigid	Commercial gel type	O
17	X	X (No real-time classification)	X	X	2	Elbow extension/ flexion	Rigid	Commercial gel type	X
15	X	X	X	X	2	Elbow extension/flexion	No sensor used	No sensor used	No sensor used
7	X	X	X	O	1	Elbow flexion	Rigid	Commercial gel type	O
8	X	X	X	O	1	Elbow flexion	Rigid	Commercial gel type	X
38	X	X	X	O	2	Elbow extension/ flexion	Rigid	Commercial gel type	X
19	X	X	X	O	1	Vertical shoulder flexion	No sensor used	No sensor used	No sensor used
6	X	X	X	O	3	Vertical shoulder flexion/elbow extension/ flexion	Rigid	Commercial gel type	X
9	X	X	X	O	2	Vertical shoulder flexion/elbow flexion	Rigid	Commercial gel type	X
14	X	X	X	O	2	Shoulder abduction/ Elbow flexion	Rigid	Commercial gel type	O
11	X	X	X	O	2	Vertical shoulder flexion/elbow flexion	Rigid	Commercial gel type	X
12	X	X	X	O	2	Vertical shoulder flexion/elbow flexion	Rigid	Commercial gel type	X
13	X	X	X	O	1	Shoulder abduction	Rigid	Commercial gel type	O
5	X	X	X	X	1	Elbow flexion	Rigid	Commercial gel type	X
10	X	X	X	X	3	Vertical shoulder flexion/elbow extension/ flexion	Rigid	Commercial gel type	X

4	X	X	X	X	1	Elbow flexion	No sensor used	No sensor used	No sensor used
---	---	---	---	---	---	---------------	----------------	----------------	----------------

\*Integrated system means the integration of sensory feedback and human intention predicting algorithm into the exoskeleton robotics

## Supplementary Information

### Intelligent upper-limb exoskeleton using deep learning to predict human intention for sensory-feedback augmentation

Jinwoo Lee<sup>1,2,†</sup>, Kangkyu Kwon<sup>2,3,†</sup>, Ira Soltis<sup>2,4,†</sup>, Jared Matthews<sup>2,4</sup>, Yoon-Jae Lee<sup>2,3</sup>, Hojoong Kim<sup>2,4</sup>, Lissette Romero<sup>2,5</sup>, Nathan Zavanelli<sup>2,3</sup>, Youngjin Kwon<sup>2,4</sup>, Shinjae Kwon<sup>2,4</sup>, Jimin Lee<sup>2,4</sup>, Yewon Na<sup>2,4</sup>, Sung Hoon Lee<sup>2,3</sup>, Ki Jun Yu<sup>6</sup>, Minoru Shinohara<sup>2,7,8</sup>, Frank L. Hammond<sup>4,8</sup>, Woon-Hong Yeo<sup>2,4,8,9\*</sup>

<sup>1</sup> Department of Mechanical, Robotics, and Energy Engineering, Dongguk University, Seoul, 04620, Republic of Korea

<sup>2</sup> IEN Center for Human-Centric Interfaces and Engineering, Institute for Electronics and Nanotechnology, Georgia Institute of Technology, Atlanta, GA 30332, USA

<sup>3</sup> School of Electrical and Computer Engineering, Georgia Institute of Technology, Atlanta, GA 30332, USA

<sup>4</sup> George W. Woodruff School of Mechanical Engineering, Georgia Institute of Technology, Atlanta, GA 30332, USA

<sup>5</sup> School of Industrial Design, Georgia Institute of Technology, Atlanta, GA 30332, USA

<sup>6</sup> School of Electrical and Electronic Engineering, Yonsei University, Seoul 03722, Republic of Korea

<sup>7</sup> School of Biological Sciences, Georgia Institute of Technology, Atlanta, GA 30332, USA

<sup>8</sup> Wallace H. Coulter Department of Biomedical Engineering, Georgia Institute of Technology and Emory University School of Medicine, Atlanta, GA 30332, USA

<sup>9</sup> Institute for Materials, Parker H. Petit Institute for Bioengineering and Biosciences, Neural Engineering Center, Institute for Robotics and Intelligent Machines, Georgia Institute of Technology, Atlanta, GA 30332, USA

† J. Lee, K. Kwon, and I. Soltis equally contributed to this work

\*Corresponding author. Email: Dr. Woon-Hong Yeo (whyeo@gatech.edu)

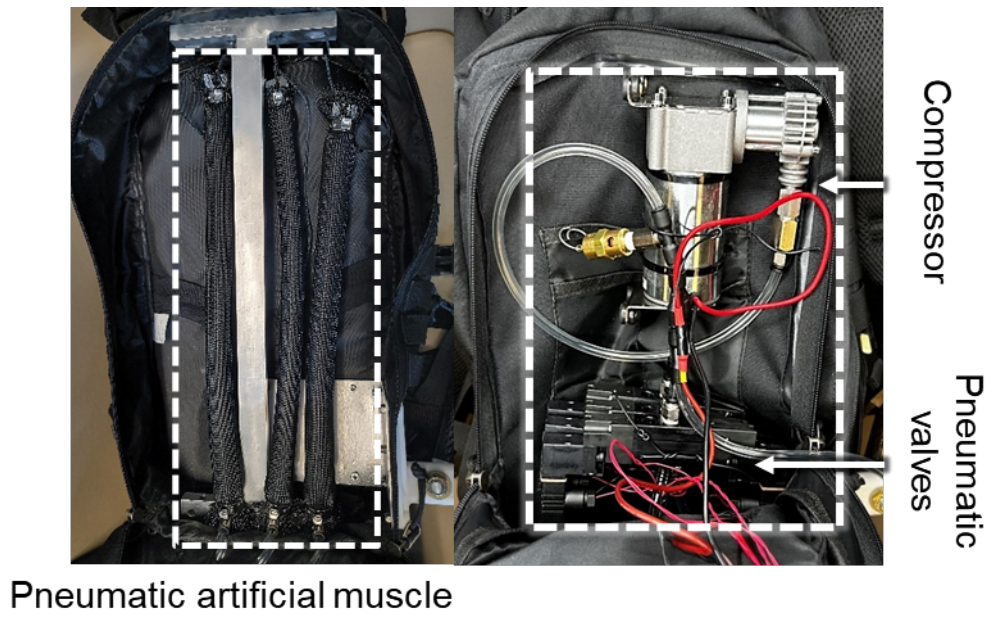


**Fig. S1.** Photograph of the backpack interior that consists of the PAM units, compressor, and pneumatic valves.

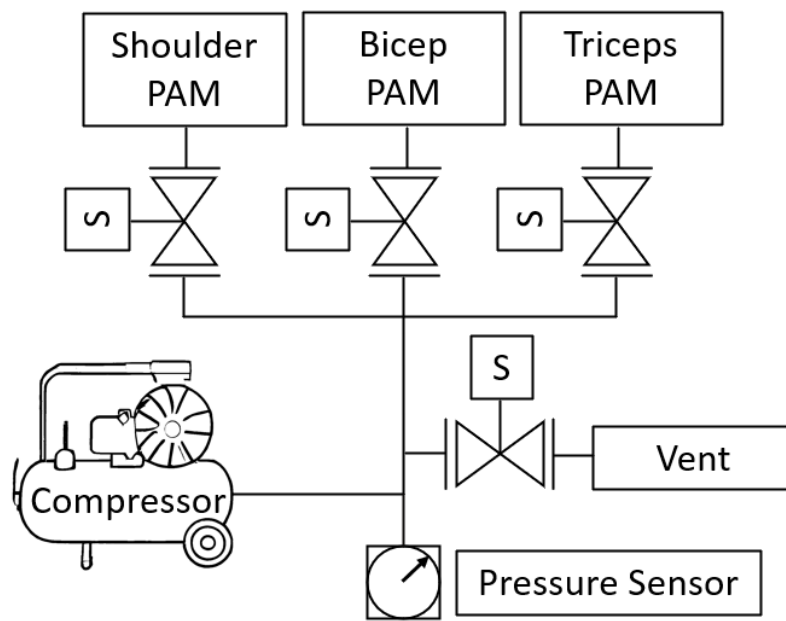


**Fig. S2.** Flow diagram that describes how PAMs are controlled with a pressor sensor and compressor.



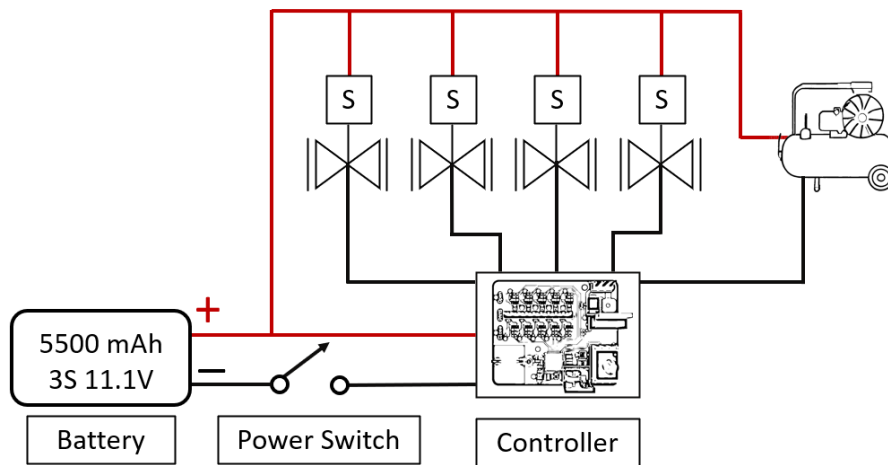


**Fig. S3.** Power diagram that explains how power is controlled and supplied to the PAM units.

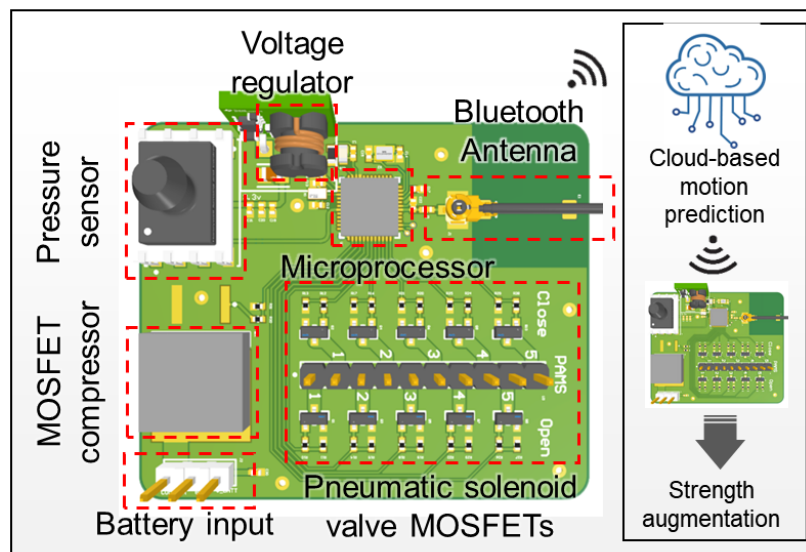
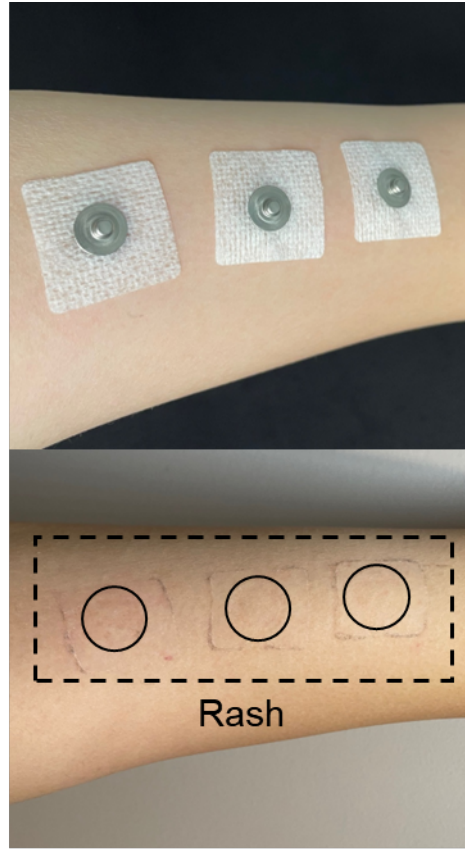


**Fig. S4.** Graphical illustration of the PCB that controls the PAM actuation.



This work



Commercial gel-type sensor

**Fig. S5.** Skin irritation comparison test between the electrode in this work and the commercial gel-type electrode

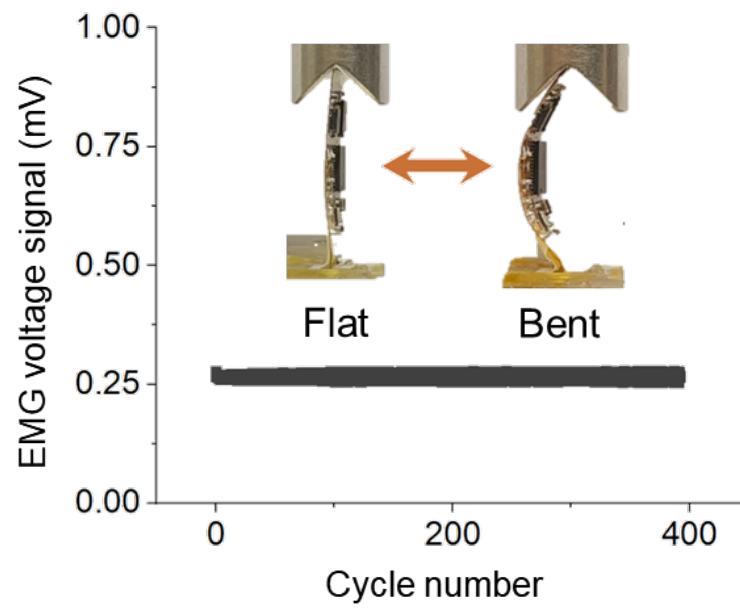


**Fig. S6.** Cyclic bending test of the flexible PCB circuit for the skin-like EMG sensor. We measured the wirelessly transmitted EMG voltage signal as this information corroborates that the PCB can deliver information under the application of mechanical stress.



**Fig. S7.** The photograph of the human upper limb with the skin-like EMG sensors attached.

### Cloud-based Android GUI application



**Fig. S8.** Screenshots of the cloud-based Android GUI that can connect wireless sensors, monitor EMG signals during training, and conduct real-time motion classification.

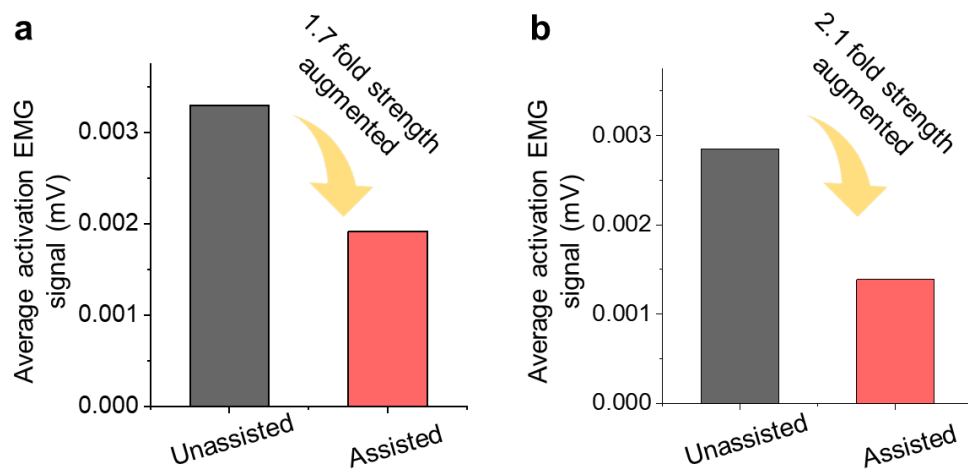


**Fig. S9.** Average activation EMG signal comparison between with and without exoskeleton assistance during (a) biceps flexion and (b) shoulder flexion.

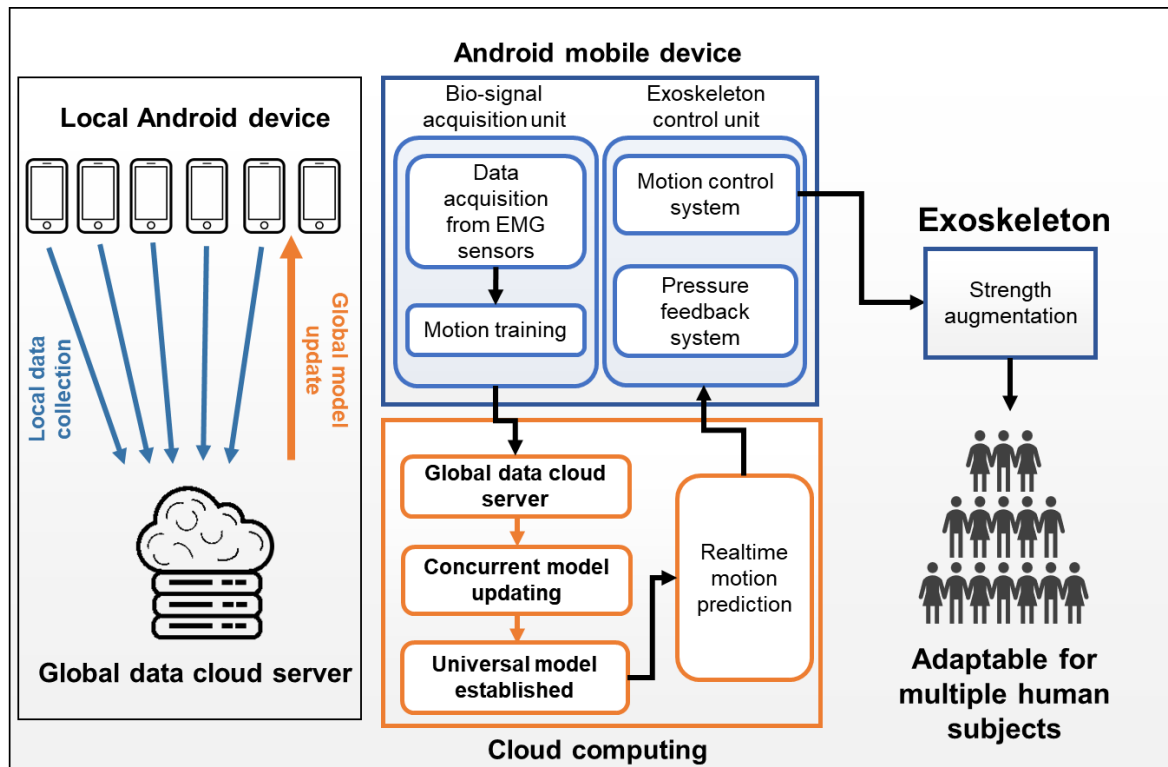


**Fig. S10.** Potential usage scheme of the cloud computing proposed in this work. Unlike the local deep-learning classification, the incorporation of cloud-computing to motion classification enables the system to receive massive amount of training data from multiple human subjects and it also allows to update the deep-learning model online at any time.



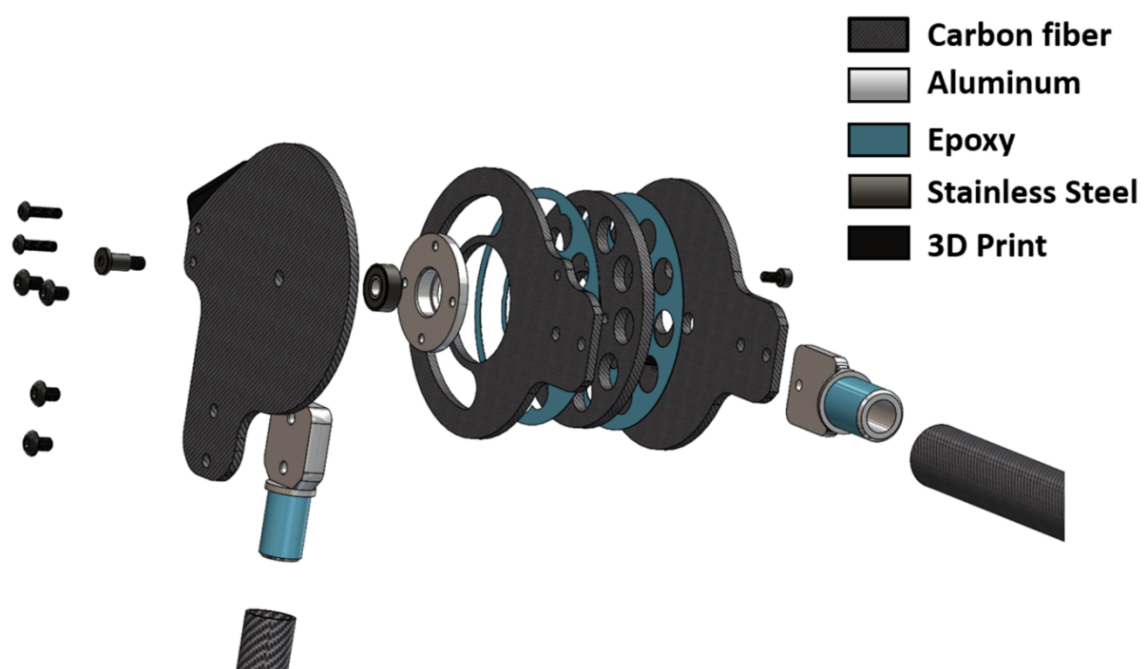


**Fig. S11.** Graphical exploded view of shoulder joint of the exoskeleton frame.

**Table S1. Weight breakdown of the exoskeleton**

Item	Individual Weight (g)	Quantity	Total Weight (g)
Solenoid Valves	149	4	596
PAM	104	3	312
PAM Frame	195	1	195
Battery	390	1	390
Cable Housing	208	1	208
Backpack	1525	1	1525
Compressor	700	1	700
PCB and PCB Case	45	1	45
Carbon Fiber Structure	670	1	670
Sum of Components (Minus wiring, tubing and some 3D printed parts)			5141
Total Weight (As Measured)			4780
Miscellaneous Wiring, Tubing and Hardware			139

**Table S2. Machine learning layer information for biceps activation classification.** Detailed information about the layers of proposed biceps network for biceps motion classification.

Layer	Output	# filter	Kernel size	Option
Input	502×1			
Conv1D-1_1	502×6	6	3	Padding = Same Activation = LeakyReLu
Conv1D-1_2	502×4	4	4	Padding = Same Activation = LeakyReLu
BatchNorm	502×4			
MaxPool1D-1	125×4		4	
Conv1D-2_1	125×4	38	3	Padding = Same Activation = LeakyReLu
Conv1D-2_2	125×4	4	4	Padding = Same Activation = LeakyReLu
BatchNorm	125×4			
MaxPool1D-2	31×4		4	
LSTM	31×4	4		return_sequences = True Activation = tanh
Flatten_1	124			
Flatten_2	432			
Dropout	432			$\rho = 0.30$
Flatten_final	3			Activation = softmax
Output_sub	3			
Data_Fusion	6			

**Table S3. Machine learning layer information for triceps activation classification.** Detailed information about the layers of proposed triceps network for triceps motion classification.

Layer	Output	# filter	Kernel size	Option
Input	502×1			
Conv1D-1_1	502×50	50	3	Padding = Same Activation = LeakyReLu
Conv1D-1_2	502×4	4	4	Padding = Same Activation = LeakyReLu
BatchNorm	502×4			
MaxPool1D-1	125×4		4	
Conv1D-2_1	125×2	50	2	Padding = Same Activation = LeakyReLu
Conv1D-2_2	125×4	4	4	Padding = Same Activation = LeakyReLu
BatchNorm	125×4			
MaxPool1D-2	31×4		4	
LSTM	31×4	4		return_sequences = True Activation = tanh
Flatten_1	124			
Flatten_2	272			
Dropout	272			$\rho = 0.30$
Flatten_final	3			Activation = softmax
Output_sub	3			
Data_Fusion	6			

**Table S4. Machine learning layer information for latissimus dorsi activation classification.**  
Detailed information about the layers of proposed latissimus dorsi network for shoulder motion classification.

Layer	Output	# filter	Kernel size	Option
Input	502×1			
Conv1D-1_1	502×58	58	3	Padding = Same Activation = LeakyReLu
Conv1D-1_2	502×4	4	4	Padding = Same Activation = LeakyReLu
BatchNorm	502×4			
MaxPool1D-1	125×4		4	
Conv1D-2_1	125×2	54	3	Padding = Same Activation = LeakyReLu
Conv1D-2_2	125×4	4	4	Padding = Same Activation = LeakyReLu
BatchNorm	125×4			
MaxPool1D-2	31×4		4	
LSTM	31×4	4		return_sequences = True Activation = tanh
Flatten_1	124			
Flatten_2	496			
Dropout	496			$\rho = 0.30$
Flatten_final	3			Activation = softmax
Output_sub	3			
Data_Fusion	6			

**Table S5. Machine learning layer information for medial deltoids activation classification.**  
Detailed information about the layers of proposed medial deltoids network for shoulder motion classification.

Layer	Output	# filter	Kernel size	Option
Input	502×1			
Conv1D-1_1	502×10	10	3	Padding = Same Activation = LeakyReLu
Conv1D-1_2	502×4	4	4	Padding = Same Activation = LeakyReLu
BatchNorm	502×4			
MaxPool1D-1	125×4		4	
Conv1D-2_1	125×2	2	2	Padding = Same Activation = LeakyReLu
Conv1D-2_2	125×4	4	4	Padding = Same Activation = LeakyReLu
BatchNorm	125×4			
MaxPool1D-2	31×4		4	
LSTM	31×4	4		return_sequences = True Activation = tanh
Flatten_1	124			
Flatten_2	496			
Dropout	496			$\rho = 0.30$
Flatten_final	3			Activation = softmax
Output_sub	3			
Data_Fusion	6			